

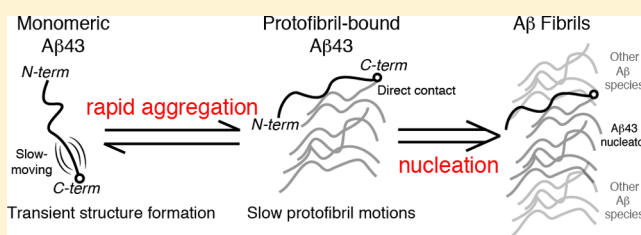
# The C-Terminal Threonine of A $\beta$ 43 Nucleates Toxic Aggregation via Structural and Dynamical Changes in Monomers and Protofibrils

Alexander E. Conicella<sup>†</sup> and Nicolas L. Fawzi<sup>\*‡</sup>

<sup>†</sup>Graduate Program in Molecular Biology, Cell Biology, and Biochemistry and <sup>‡</sup>Department of Molecular Pharmacology, Physiology, and Biotechnology, Brown University, Providence, Rhode Island 02912, United States

## Supporting Information

**ABSTRACT:** Recent studies suggest that deposition of amyloid  $\beta$  ( $A\beta$ ) into oligomeric aggregates and fibrils, hallmarks of Alzheimer's disease, may be initiated by the aggregation of  $A\beta$  species other than the well-studied 40- and 42-residue forms,  $A\beta$ 40 and  $A\beta$ 42, respectively. Here we report on key structural, dynamic, and aggregation kinetic parameters of  $A\beta$ 43, extended by a single threonine at the C-terminus relative to  $A\beta$ 42. Using aggregation time course experiments, electron microscopy, and a combination of nuclear magnetic resonance measurements including backbone relaxation, dark-state exchange saturation transfer, and quantification of chemical shift differences and scalar coupling constants, we demonstrate that the C-terminal threonine in  $A\beta$ 43 increases the rate and extent of protofibril aggregation and confers slow C-terminal motions in the monomeric and protofibril-bound forms of  $A\beta$ 43. Relative to the neighboring residues, the hydrophilic Thr43 of  $A\beta$ 43 favors direct contact with the protofibril surface more so than the C-terminus of  $A\beta$ 40 or  $A\beta$ 42. Taken together, these results demonstrate the potential of a small chemical modification to affect the properties of  $A\beta$  structure and aggregation, providing a mechanism for the potential role of  $A\beta$ 43 as a primary nucleator of  $A\beta$  aggregates in Alzheimer's disease.



The triggers for the aberrant formation of extracellular plaques of the amyloid  $\beta$  ( $A\beta$ ) peptide and intracellular neurofibrillary tangles of the protein tau remain as critical unanswered questions in Alzheimer's disease (AD) research. Although the amyloid cascade hypothesis posits that the aggregation-prone  $A\beta$  peptides are the causative agents in AD,<sup>1</sup> deposition of  $A\beta$  into the ordered amyloid fibrils that are the primary component of plaques correlates only weakly with disease severity.<sup>2</sup> Subsequent studies have suggested therefore that the primary toxic species in AD are lower-molecular weight aggregates of  $A\beta$  lacking the highly organized structure of amyloid fibrils.<sup>3</sup> Supporting this hypothesis, numerous studies have demonstrated that soluble  $A\beta$  aggregates, including both oligomers (aggregates consisting of 2–20 peptides) and protofibrils (intermediates on the amyloid fibril formation pathway consisting of hundreds of peptides), are neurotoxic in cell culture and their presence correlates with the progression of AD.<sup>4,5</sup> Definitive proof of the “toxic oligomer” hypothesis has yet to emerge, however, hampered by a critical lack of clarity regarding the mechanism of neuronal toxicity and the structures of the diverse array of nonfibrillar assemblies of  $A\beta$  formed *in vivo* and even *in vitro*,<sup>6</sup> motivating efforts to characterize the structural details of the assembly process.

Formed by progressive proteolytic cleavage of the amyloid precursor protein (APP),  $A\beta$  peptides are found in lengths ranging from 39 to 49 amino acids.<sup>7</sup>  $A\beta$ 40 and  $A\beta$ 42 are the primary products of the stepwise cleavage by  $\gamma$ -secretase of the C99 C-terminal fragment of APP along two lineages:  $A\beta$ 49  $\rightarrow$   $A\beta$ 46  $\rightarrow$   $A\beta$ 43  $\rightarrow$   $A\beta$ 40  $\rightarrow$   $A\beta$ 38/37 and  $A\beta$ 48  $\rightarrow$   $A\beta$ 45  $\rightarrow$

$A\beta$ 42  $\rightarrow$   $A\beta$ 39.<sup>8</sup>  $A\beta$ 40, the most abundant, 40-amino acid form, is significantly less prone to aggregation than  $A\beta$ 42, the 42-amino acid form extended at the C-terminus by two hydrophobic residues, isoleucine and alanine.<sup>9</sup> Mutations in APP that result in higher ratios of  $A\beta$ 42 to  $A\beta$ 40 cause familial Alzheimer's disease (FAD), underscoring the connection between the aggregation propensity of the C-terminal region of  $A\beta$  and the occurrence of AD.<sup>10</sup> Although  $A\beta$  peptides are primarily unstructured as monomers, NMR experiments probing backbone and side chain dynamics have demonstrated that  $A\beta$ 42 has a more rigid C-terminal region compared to that of  $A\beta$ 40,<sup>11–13</sup> suggesting that slower motions in this region contribute to the enhanced aggregation propensity of  $A\beta$ 42. Recent technical advances have made it possible to characterize the structure of both fibrillar<sup>14–16</sup> and nonfibrillar (oligomeric and protofibrillar) aggregates<sup>17–24</sup> of  $A\beta$  and their interactions with monomeric  $A\beta$ <sup>25</sup> with atomistic resolution despite the challenges associated with the large size, disordered structure, and transient nature of aggregates. Using dark-state exchange saturation transfer (DEST) NMR to probe the atomic-resolution structure and dynamics of peptides within cytotoxic  $A\beta$  protofibrillar aggregates ranging from 2 to 20 MDa lacking the linear, unbranched ordered structure of mature amyloid fibrils, we have recently demonstrated that the two additional

Received: January 30, 2014

Revised: April 25, 2014

Published: April 28, 2014

residues in A $\beta$ 42 significantly slow motions across the entire C-terminal region of A $\beta$ 42 (residues 31–42) in the protofibril-bound state, suggesting that slowed motions may contribute to aggregation propensity.<sup>26</sup>

Although the toxicity of oligomeric forms of A $\beta$  and their presence in disease are well-established, the trigger for the formation of toxic oligomers from the constitutively present A $\beta$  peptides is unknown. Recently, several studies have demonstrated that other A $\beta$  variants, including N-terminally truncated pyroglutamate-modified A $\beta$  (e.g., pE3-42) and extended C-terminal forms (e.g., A $\beta$ 43), may be more prone to aggregation than A $\beta$ 42 and may play a critical role in AD by nucleating A $\beta$  aggregation.<sup>27,28</sup> Bearing a single additional threonine at the C-terminus relative to A $\beta$ 42, A $\beta$ 43 appears more frequently in AD amyloid plaques than A $\beta$ 40<sup>29</sup> despite a 1000-fold lower cortical concentration.<sup>30</sup> A $\beta$ 43 is enriched 20- and 40-fold in the frontal and occipital cortices, respectively, of patients with sporadic AD compared to nondiseased controls, twice the enrichment of A $\beta$ 42 and 1 order of magnitude more enriched than A $\beta$ 40.<sup>30</sup> In a transgenic APP-expressing mouse model of AD, A $\beta$ 43 is the earliest depositing A $\beta$  species, suggesting A $\beta$ 43 plays a crucial role in the early stages of AD progression as a nucleator of A $\beta$  aggregates.<sup>31</sup> Previous studies have demonstrated that A $\beta$ 43 has aggregation properties similar to those of A $\beta$ 42,<sup>28,32</sup> yet A $\beta$ 43 is significantly more neurotoxic when applied to cells in culture.<sup>28</sup> Furthermore, earlier onset of memory impairment, neuropathology, and plaque formation is observed in a mouse model of AD in which a knock-in  $\gamma$ -secretase bearing an FAD mutation increases the level of A $\beta$ 43 production without changing A $\beta$ 42 levels.<sup>28</sup>

Given the demonstrated potential of A $\beta$ 43 to be a nucleator of toxic aggregates in AD, several important open questions remain regarding the biophysical chemistry of A $\beta$ 43. Is A $\beta$ 43 more prone to forming toxic aggregates than A $\beta$ 42? If so, why does the addition of a hydrophilic amino acid at the C-terminus of A $\beta$  lead to greater aggregation propensity typically associated with hydrophobically driven self-association? A clear understanding of the biophysical properties of A $\beta$ 43 and its aggregates will provide insight into its involvement in AD and serve as critical data for a potential target for future AD therapeutics. In this study, we characterize the monomeric and protofibril-bound states of A $\beta$ 43 under conditions that stabilize protofibrils using solution NMR experiments sensitive to both the structure and motions of A $\beta$  peptides, properties that are known to distinguish the aggregation propensity of shorter A $\beta$  variants. By demonstrating that the additional C-terminal threonine speeds and enhances protofibril formation, alters the C-terminal monomer structural ensemble, and contributes to slower motions of the peptide in both the monomeric and protofibril-bound states, we provide a detailed characterization of the aggregation and structural properties of A $\beta$ 43 that contribute to its unique role in AD.

## MATERIALS AND METHODS

**Preparation of A $\beta$  Samples.** Uniformly <sup>15</sup>N-labeled A $\beta$ 43, A $\beta$ 42, and A $\beta$ 40 were purchased from rPeptide (Bogart, GA). To remove preformed aggregates, samples were prepared from NaOH-treated lyophilized stocks as described previously.<sup>26</sup> A $\beta$ 43 samples were diluted to concentrations of 120, 25, and 15  $\mu$ M in 50 mM HEPES (pH 6.8) and a 90% H<sub>2</sub>O/10% D<sub>2</sub>O mixture and maintained at 10 °C at all times unless otherwise noted. Protofibril formation of 120  $\mu$ M A $\beta$ 43 was monitored using a time course of <sup>1</sup>H–<sup>15</sup>N heteronuclear single-quantum

coherence (HSQC) correlation spectra cross peak intensities. Establishment of an equilibrium between monomers and protofibrils (i.e., <10% change per day in the concentration of monomers as measured by monomer resonance intensities) in 120  $\mu$ M A $\beta$ 43 samples occurred between 24 and 48 h, and NMR experiments characterizing monomer–protofibril interaction were performed after this point. For characterization of transverse relaxation rates and scalar coupling constants of monomeric A $\beta$  peptides, 25  $\mu$ M A $\beta$ 42 and 50  $\mu$ M A $\beta$ 40 were prepared as described above. Measurements of <sup>1</sup>H–<sup>13</sup>C HSQC at natural abundance <sup>13</sup>C were taken in 20 mM sodium phosphate (pH 6.8) to prevent <sup>13</sup>C signals arising from HEPES buffer.

To investigate the effects of secondary structure on A $\beta$  chemical shifts and R<sub>2</sub> values, we prepared lyophilized stocks of <sup>15</sup>N-labeled A $\beta$ 43 and A $\beta$ 42 as described above and diluted them to 100  $\mu$ M in 7.2 M urea, 50 mM HEPES (pH 6.9), and a 95% H<sub>2</sub>O/5% D<sub>2</sub>O mixture.

**Electron Microscopy.** Aliquots for transmission electron microscopy (TEM) studies were taken from 120  $\mu$ M A $\beta$ 43 NMR samples and diluted to 165 nM with 50 mM HEPES (pH 6.8) and a 90% H<sub>2</sub>O/10% D<sub>2</sub>O mixture. Four microliters of the diluted A $\beta$ 43 solution was immediately spotted onto an ultrathin carbon film on holey carbon support grids (product code 01824, Ted Pella, Reading, CA), washed three times with deionized H<sub>2</sub>O, stained with 5  $\mu$ L of 3% uranyl acetate (Electron Microscopy Sciences, Hatfield, PA) for 60 s, blotted, and left to air-dry. TEM sample grids were then imaged with a Philips 410 transmission electron microscope.

**Solution NMR Experiments.** All NMR experiments were recorded at 10 °C using a Bruker Avance III HD NMR spectrometer operating at a <sup>1</sup>H frequency of 850 MHz equipped with a Bruker TCI z-axis gradient cryogenic probe. Experimental sweep widths and acquisition times (i.e., resolution) and the number of transients were optimized for the necessary resolution, experiment time, and signal-to-noise ratio for each experiment type but kept constant for the same experiment conducted with different peptide (i.e., A $\beta$ 40, A $\beta$ 42, and A $\beta$ 43) samples and different concentration conditions.

To measure the difference in transverse relaxation rates in the presence and absence of A $\beta$ 43 protofibrils, in-phase <sup>15</sup>N transverse relaxation rates (<sup>15</sup>N R<sub>2</sub>) were measured for A $\beta$ 43 at 120 and 25  $\mu$ M with an interleaved Carr–Purcell–Meiboom–Gill (CPMG) experiment (hsqc2etf3gpsi3d, Topspin version 3.2, Bruker). Each interleaved experiment comprises 90\* and 1360\* complex data pairs in the indirect <sup>15</sup>N and direct <sup>1</sup>H dimensions, respectively, with corresponding acquisition times of 66 and 160 ms and sweep widths of 15.8 and 10 ppm centered at 119 and 4.9 ppm, respectively. A CPMG field of 556 Hz was used for all transverse relaxation measurements with total R<sub>2</sub> relaxation CPMG loop lengths of 16.4, 32.9, 65.7, 131.4, 197.2, and 295.7 ms. An interscan delay of 2.5 s was used. Data were processed with nmrPipe<sup>33</sup> as follows. Data were apodized with a 10 Hz Gaussian function for the <sup>1</sup>H dimension and a cosine bell function for the <sup>15</sup>N dimension. To resolve peaks for residues D7 and D23 only, spectra were additionally processed separately with the following change: free induction decays were apodized with a 2 Hz exponential line broadening for the <sup>1</sup>H dimension. Best-fit R<sub>2</sub> relaxation rates were calculated by least-squares optimization of <sup>1</sup>H/<sup>15</sup>N peak intensities to single-exponential decay functions. Given the low NMR signal intensity due to only ~12  $\mu$ M A $\beta$ 43 remaining monomeric at a total concentration of 120  $\mu$ M,

independent measurements of  $R_2$  were recorded, and the resulting transverse relaxation rates were averaged.  $\Delta R_2$ , the difference in  $^{15}\text{N}$   $R_2$  values in the presence (120  $\mu\text{M}$ ) and absence (25  $\mu\text{M}$ ) of protofibrils, was then calculated.

Dynamical differences in monomeric (15 and 25  $\mu\text{M}$  samples)  $A\beta 42$  and  $A\beta 43$  were observed by measurement of  $^{15}\text{N}$   $R_1$ , temperature-compensated  $^{15}\text{N}$   $R_2$ , and heteronuclear NOE experiments using standard pulse sequences (hsqct1etf3gpsi3d, hsqct2etf3gpsi3d, and hsqcnoef3gpsi, respectively, from Topspin version 3.2). Each  $R_2$  experiment comprised six interleaved CPMG  $^{15}\text{N}$   $R_2$  relaxation times of 16.4, 49.3, 82.2, 131.4, 197.2, and 263.7 ms at a CPMG field strength of 556 Hz. Each interleaved two-dimensional experiment comprised 128\* and 1360\* complex data points in the indirect  $^{15}\text{N}$  and direct  $^1\text{H}$  dimensions, respectively, with corresponding acquisition times of 94 and 160 ms and sweep widths of 15.8 and 10 ppm centered at 119 and 4.9 ppm, respectively. Experiments were conducted with 16 transients per free induction decay and an interscan delay of 2.5 s, resulting in a total experiment time of 2 days. Data were processed as described above. Each  $R_1$  experiment comprised seven interleaved  $^{15}\text{N}$   $R_1$  relaxation times of 100, 200, 300, 400, 600, 800, and 1000 ms, with acquisition and processing parameters identical to those described for  $R_2$ . Heteronuclear NOE experiments were conducted with a 5 s interscan delay ( $>5T_1$  as measured), interleaving FIDs with and without saturation, and 48 transients per free induction decay, with acquisition and processing parameters identical to those described for  $R_2$ .

To determine if differences in chemical shift and  $R_2$  observed for  $A\beta 43$  and  $A\beta 42$  arise due to structural changes,  $^1\text{H}$ - $^{15}\text{N}$  HSQC spectra and temperature-compensated  $^{15}\text{N}$   $R_2$  experiments were measured for 100  $\mu\text{M}$   $A\beta 43$  and  $A\beta 42$  in 7.2 M urea, as described above. Each  $R_2$  experiment comprised six interleaved CPMG  $^{15}\text{N}$   $R_2$  relaxation time points of 16.4, 49.3, 82.2, 131.4, 197.2, and 263.7 ms at a CPMG field strength of 556 Hz. Each interleaved two-dimensional experiment comprises 128\* and 1360\* complex data points in the indirect  $^{15}\text{N}$  and direct  $^1\text{H}$  dimensions, respectively, with corresponding acquisition times of 74 and 160 ms and sweep widths of 20 and 10 ppm centered at 117.75 and 4.9 ppm, respectively. Experiments were conducted with four transients per free induction decay and an interscan delay of 2.5 s, resulting in a total experiment time of 5.5 h. Data were processed as described above.

Probing of the protofibril-bound state of  $A\beta 43$  present at 120  $\mu\text{M}$  was accomplished with dark-state exchange saturation transfer (DEST) NMR spectroscopy using a series of interleaved, HSQC-based experiments.<sup>26,34</sup> Briefly, initial  $^1\text{H}$  magnetization is transferred to  $^{15}\text{N}_z$  by a refocused INEPT element, preferentially saturated in the protofibril-bound state by 400 ms  $^{15}\text{N}$  radiofrequency (RF) continuous wave pulses applied at a power of 500 or 375 Hz and  $^{15}\text{N}$  carrier frequency offsets between 6 and  $-6$  kHz (for 500 Hz, 6, 4, 2.5,  $-2.5$ ,  $-4$ , and  $-6$  kHz offsets; for 375 Hz, 4, 2.5, and  $-2.5$  kHz offsets; three reference experiments with no applied RF field), transferred to the NMR-visible monomeric species by chemical exchange, and detected after INEPT transfer to  $^1\text{H}$ . Each interleaved two-dimensional experiment comprises 90\* and 2048\* complex data points in the indirect  $^{15}\text{N}$  and direct  $^1\text{H}$  dimensions, respectively, with corresponding acquisition times of 66 and 229 ms and sweep widths of 15.8 and 10.5 ppm centered around 119 and 4.9 ppm, respectively. Data were

processed as described above. Attenuation of the NMR signal due to dark-state exchange saturation transfer of each resonance was normalized to the average intensity of each resonance in the three interleaved reference experiments (with no RF power).

**Quantification of Spectral Differences between Monomeric  $A\beta 42$  and  $A\beta 43$ .** Chemical shift differences between  $A\beta 42$  and  $A\beta 43$  monomers were obtained from  $^1\text{H}$ - $^{15}\text{N}$  HSQC experiments measured at 10 and 37  $^\circ\text{C}$ . Each experiment comprised 64\* and 2048\* complex data points in the indirect  $^{15}\text{N}$  and direct  $^1\text{H}$  dimensions, respectively, with corresponding acquisition times of 31 and 229 ms and sweep widths of 24 and 10.5 ppm centered at 119 and 4.9 ppm (4.7 ppm at 37  $^\circ\text{C}$ ), respectively. Experiments were conducted with eight transients per free induction decay. Data were processed as described above. To resolve the overlap for residues D7, A21, V24, I31, I32, and M35, direct  $^1\text{H}$  dimension data were separately processed with 1 Hz exponential line broadening.

$^1\text{H}$ - $^{13}\text{C}$  HSQC experiments conducted at 10  $^\circ\text{C}$  comprised 256\* and 1024\* complex data points in the  $^{13}\text{C}$  and direct  $^1\text{H}$  dimensions, respectively, with 96 transients per free induction decay. Data were processed as described above.

For 100  $\mu\text{M}$   $A\beta 43$  and  $A\beta 42$  samples prepared in 7.2 M urea, chemical shift differences were quantified from similar  $^1\text{H}$ - $^{15}\text{N}$  HSQC experiments. Each experiment comprised 128\* and 2048\* complex data points in the indirect  $^{15}\text{N}$  and direct  $^1\text{H}$  dimensions, respectively, with corresponding acquisition times of 62 and 229 ms and sweep widths of 24 and 10.5 ppm centered at 119 and 4.9 ppm, respectively. Experiments were conducted with two transients per free induction decay. Data were processed as described above, with 6.5 Hz Gaussian line broadening in the direct  $^1\text{H}$  dimension.

$^3J_{\text{HN-H}\alpha}$  scalar coupling constants for 50  $\mu\text{M}$   $A\beta 40$ , 25  $\mu\text{M}$   $A\beta 42$ , and 25  $\mu\text{M}$   $A\beta 43$  were obtained from alternate processing of the high-signal-to-noise ratio HSQC experiment derived from a  $^{15}\text{N}$   $R_2$  relaxation time point (16.4 ms) of the temperature-compensated  $^{15}\text{N}$   $R_2$  experiments (see above) for 10  $^\circ\text{C}$  values, and from HSQC spectra (see above) for 37  $^\circ\text{C}$  values. Free induction decays were apodized with 1 Hz exponential line broadening in the direct  $^1\text{H}$  dimension, and a cosine bell function in the indirect  $^{15}\text{N}$  dimension.  $^3J_{\text{HN-H}\alpha}$  values were determined by line-shape analysis using a custom script in the software program R where the center position, widths, and intensities of two Lorentzian functions were best fit to the  $^1\text{H}$  dimension slices for the resonances corresponding to each backbone  $^1\text{H}$ - $^{15}\text{N}$  pair.

**DEST Model Fitting.** Kinetic and dynamic parameters describing  $A\beta 43$  monomer–protofibril interactions and the  $A\beta 43$  protofibril-bound state were derived from experimental NMR data with DESTfit as previously described.<sup>34</sup> Briefly, DESTfit was run with a pseudo-two-state fit type with the apparent first-order association rate constant ( $k_{\text{on}}^{\text{app}}$ ) set to the maximal observed  $\Delta R_2$ , as previously conducted in the analysis of DEST data for  $A\beta 40$  and  $A\beta 42$ .<sup>26,34</sup>

## RESULTS

**$A\beta 43$  Assembles into Protofibrils Faster and to a Greater Extent Than  $A\beta 42$  or  $A\beta 40$ .** To determine the *in vitro* aggregation properties of  $A\beta 43$ ,  $^1\text{H}$ - $^{15}\text{N}$  HSQC peak intensities of resolved resonances (Figure 1) were monitored as a function of time for  $^{15}\text{N}$ -labeled  $A\beta 43$  (120 and 25  $\mu\text{M}$ ). At low concentrations (25  $\mu\text{M}$ ),  $A\beta 43$  aggregation is minimal and  $A\beta 43$  remains  $\approx 95\%$  monomeric after 2 days. However, at a



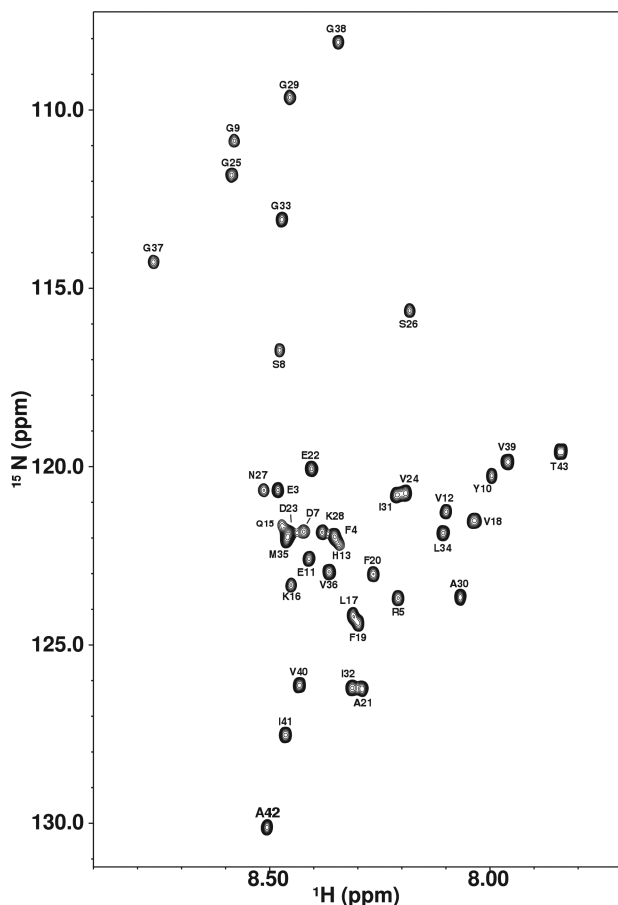


**Figure 1.** Backbone amide region of  $^1\text{H}$ - $^{15}\text{N}$  heteronuclear single-quantum coherence (HSQC) spectrum of  $25\ \mu\text{M}$   $\text{A}\beta 43$ .

higher concentration ( $120\ \mu\text{M}$ ),  $\text{A}\beta 43$  aggregates rapidly with the intensity of NMR signals decreasing to  $\sim 10\%$  of the original value within 1 day (Figure 2a). Transmission electron microscopy analysis of  $120\ \mu\text{M}$   $\text{A}\beta 43$  over time confirms that the loss of the monomeric  $\text{A}\beta 43$  signal intensity is concomitant with the formation of protofibrils. Protofibrils can be detected as little as 1 h after sample creation and are present at a much higher concentration after 24 h (Figure 2b,c). Although the atomic level structure and the heterogeneity of the contacts stabilizing the core of protofibrils formed by each  $\text{A}\beta$  variant are unknown,  $\text{A}\beta 43$  protofibrils are morphologically similar as determined by microscopy to those we have previously observed for  $\text{A}\beta 42$  and  $\text{A}\beta 40$ .<sup>26</sup> The rate of aggregation can be described by fitting  $^1\text{H}$ - $^{15}\text{N}$  HSQC peak intensities to the exponential decay function  $I(t)/I_0 = (1 - A_1)e^{-t/\tau_1} + A_1$ , where  $\tau_1$  is a time constant for protofibril formation and  $A_1$  is a constant representing the fraction remaining monomeric after protofibril formation reaches equilibrium. Best-fit parameters for  $\text{A}\beta 43$  protofibril formation under these conditions are as follows:  $\tau_1 = 6 \pm 1\ \text{h}$ , and  $A_1 = 10 \pm 4\%$ . This aggregation is much more rapid than for  $\text{A}\beta 40$  or  $\text{A}\beta 42$ , each of which requires  $>1$  week to complete protofibril formation under identical conditions.<sup>8</sup> Protofibril formation also proceeds to a greater extent for  $\text{A}\beta 43$ . After protofibril formation for 2 weeks, only  $12\ \mu\text{M}$  peptide remains monomeric compared to  $20\ \mu\text{M}$   $\text{A}\beta 42$  or  $120\ \mu\text{M}$   $\text{A}\beta 40$  at similar concentrations.<sup>26</sup> Therefore, the addition of T43 both accelerates, and decreases the critical concentration for,  $\text{A}\beta$  protofibril formation. At  $37\ ^\circ\text{C}$ , samples at concentrations of  $25\ \mu\text{M}$  that are stable at  $10\ ^\circ\text{C}$  rapidly

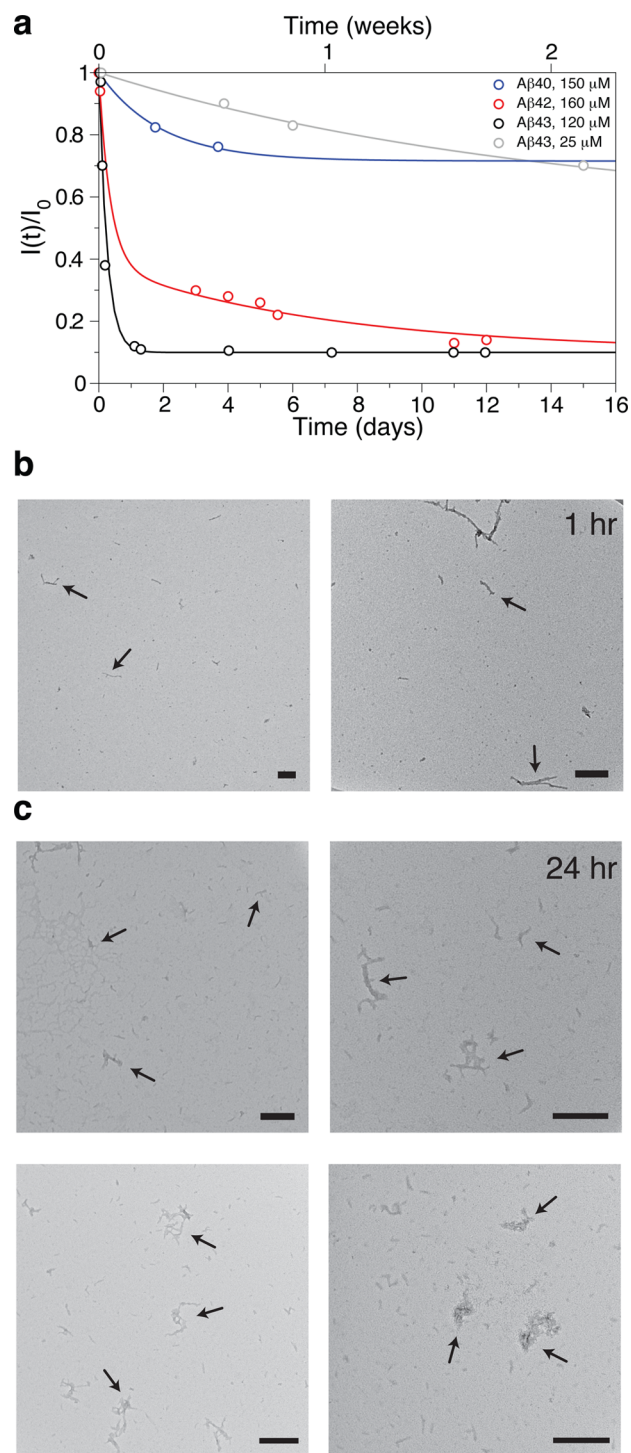


**Figure 2.**  $\text{A}\beta 43$  aggregates into protofibrillar species in a concentration-dependent and time-dependent manner. (a) The ratio of monomeric NMR signal intensity  $[I(t)/I_0]$  decays exponentially as a function of time.  $\text{A}\beta 43$  at concentrations of  $25\ \mu\text{M}$  (gray) and  $120\ \mu\text{M}$  (black) was monitored via HSQC cross peak intensities for over 2 weeks. The significantly slower aggregation of similar concentrations of  $\text{A}\beta 42$  ( $160\ \mu\text{M}$ , red) and  $\text{A}\beta 40$  ( $150\ \mu\text{M}$ , blue) under identical conditions is shown for comparison (data for  $\text{A}\beta 40$  and  $\text{A}\beta 42$  from ref 26). Transmission electron microscopy images of  $120\ \mu\text{M}$   $\text{A}\beta 43$  showing that (b) protofibrils are visible as little as 1 h after sample preparation and (c) protofibrils are present at a higher concentration after 24 h. Arrows highlight some of the protofibrils present, although many more are evident within each image. Scale bars represent  $200\ \text{nm}$ .

aggregate (Figure S1 of the Supporting Information) into micrometer length fibrillar structures much larger than the protofibrils formed at higher concentrations at 10 °C, consistent with observations that low-temperature conditions stabilize not only the monomer but also the protofibrillar intermediates.<sup>26</sup> As observed for aggregation at 10 °C, faster rates of monomer signal decay are observed for A $\beta$ 43 ( $\tau_1 = 0.45 \pm 0.02$  h, and  $A_1 = 12 \pm 1\%$ ) than for A $\beta$ 42 ( $\tau_1 = 0.94 \pm 0.17$  h, and  $A_1 = 23 \pm 5\%$ ).

**C-Terminal Motions of A $\beta$ 43 Monomers Slowed Compared to Those of A $\beta$ 42 Monomers.** The following series of NMR experiments characterizing the structure and dynamics of the monomeric and protofibril-bound states of A $\beta$ 43 compared to A $\beta$ 42 (Figure 3) provides a rationale for

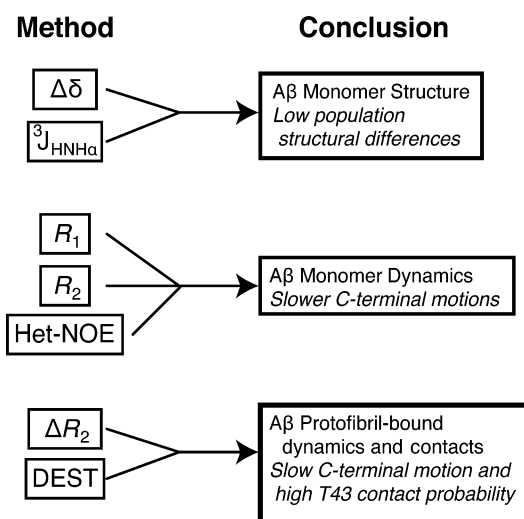


**Figure 3.** Diagram of the NMR experiments conducted, the phenomena probed by these experiments, and a summary of the results.

how the addition of T43 results in the observed differences in aggregation. Fast (picosecond to nanosecond) time scale motions of the backbone positions of monomeric A $\beta$ 43 were compared to those of A $\beta$ 42 to determine if slower peptide dynamics contribute to the increased aggregation propensity of A $\beta$ 43, as observed by Wang and co-workers for A $\beta$ 40 and A $\beta$ 42.<sup>12</sup> Therefore, we measured  $^{15}\text{N}$   $R_2$ ,  $^{15}\text{N}$   $R_1$ , and heteronuclear NOE for both A $\beta$ 42 and A $\beta$ 43 under identical conditions. As expected for the hydrophilic N-terminal region (residues 3–10), no significant differences were observed between relaxation parameters for A $\beta$ 43 and A $\beta$ 42, showing that the N-terminal regions of A $\beta$  behave the same regardless of C-terminal length. However,  $^{15}\text{N}$   $R_2$  values for residues 17–42 in A $\beta$ 43, encompassing the entire central and C-terminal hydrophobic regions, are significantly higher than those for A $\beta$ 42 (Figure 4a), suggesting A $\beta$ 43 has slower motions than A $\beta$ 42 across the majority of the peptide. To confirm that the observed increases in  $R_2$  values are not the result of interactions between A $\beta$ 43 monomers and spontaneously formed trace protofibrils potentially present at a concentration of 25  $\mu\text{M}$ ,  $R_2$  values were measured for freshly prepared 15  $\mu\text{M}$  A $\beta$ 43 where the concentration of any trace aggregates would be lower. Although the signal-to-noise ratio decreased and the uncertainty in  $R_2$  increased, no systematic decrease in  $R_2$  was observed for A $\beta$ 43 at 15  $\mu\text{M}$  compared to A $\beta$ 43 at 25  $\mu\text{M}$  (Figure S2 of the Supporting Information), indicating the

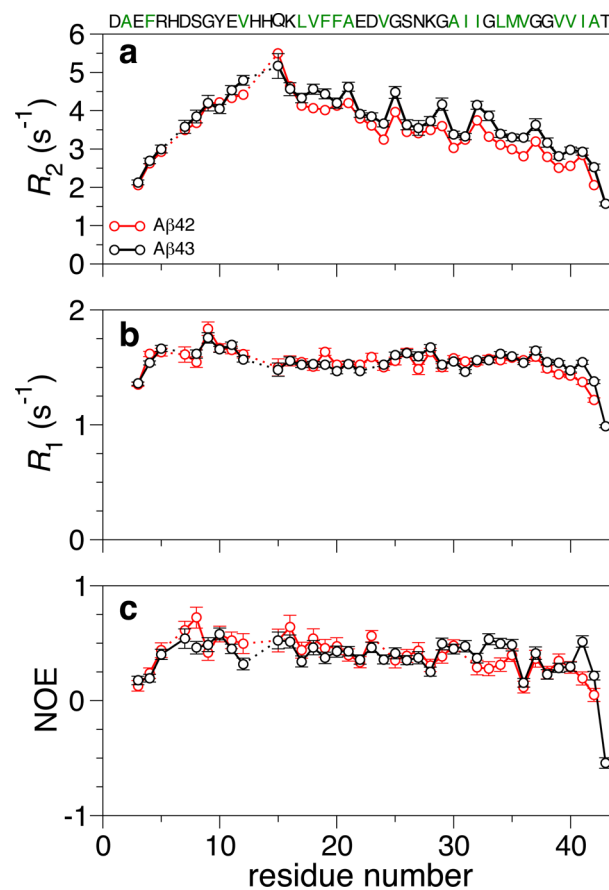


**Figure 4.** Dynamics of the backbone of monomeric A $\beta$ 42 and A $\beta$ 43 as measured by (a)  $^{15}\text{N}$   $R_2$ , (b)  $^{15}\text{N}$   $R_1$ , and (c) heteronuclear  $^{15}\text{N}$ – $\{^1\text{H}\}$  nuclear Overhauser effect (hetNOE) values. Dynamical differences on the picosecond to nanosecond time scale are observed for the central ( $R_2$ ) and C-terminal regions ( $R_2$ ,  $R_1$ , and hetNOE) of A $\beta$ 43. Error bars denote one standard deviation. Hydrophobic residues appear in green.

values at 25  $\mu\text{M}$  A $\beta$ 43 faithfully represent those of the free A $\beta$ 43 monomer.

Furthermore, significantly higher values of the heteronuclear NOE, associated with slower motions, are observed at positions 34, 35, 41, and 42 in A $\beta$ 43 (Figure 4c). In addition,  $R_1$  is significantly higher from residue 38 through the C-terminus in A $\beta$ 43 (Figure 4b) just as was previously observed in the more rigid C-terminus of A $\beta$ 42 compared to that of A $\beta$ 40.<sup>12</sup> A higher  $^{15}\text{N}$   $R_1$  is expected for slower motions under these conditions and field because of the contribution of <1 ns time scale motion to backbone relaxation in a disordered peptide.<sup>35</sup> Together,  $^{15}\text{N}$  backbone dynamics experiments confirm that dynamical differences, specifically slower motions, across the picosecond to nanosecond time scale are present in the C-terminal hydrophobic region of A $\beta$ 43 compared to that of A $\beta$ 42.

To determine whether the slower C-terminal motions observed for A $\beta$ 43 are a result of an increased propensity of A $\beta$ 43 to form stable structure or simply due to the higher molecular weight of A $\beta$ 43, we compared the  $^{15}\text{N}$   $R_2$  values in native buffer to those under denaturing conditions [100  $\mu\text{M}$  A $\beta$ 43 or A $\beta$ 42 in 7.2 M urea with the same buffer used previously, 50 mM HEPES (pH 6.9)] where any stable or transient secondary structure should be disrupted. Under denaturing conditions, the difference between  $^{15}\text{N}$   $R_2$  values for A $\beta$ 42 and A $\beta$ 43 is nearly completely suppressed (Figure S3 of the Supporting Information), suggesting that slower dynamics

observed across the central and C-terminal regions of A $\beta$ 43 under native conditions are due to the formation of transient structure.

**Structural Changes in the C-Terminal Region of Monomeric A $\beta$  Induced by T43.** To interrogate changes in structure that give rise to the observed dynamical differences, we measured the chemical shift differences between monomeric A $\beta$ 43 and A $\beta$ 42. Chemical shifts are sensitive reporters of structure and structural changes that are especially useful in systems such as A $\beta$ 43 where a low sample concentration and a disordered structural ensemble preclude characterization by traditional ( $^1\text{H}$ – $^1\text{H}$  NOE-based) NMR structural methods.<sup>36</sup> The differences between  $^1\text{H}_\text{N}$  and  $^{15}\text{N}$  chemical shift deviations ( $\Delta\delta$ ) for A $\beta$ 43 and A $\beta$ 42 were measured under native conditions. Throughout the first 20 residues, absolute  $^1\text{H}_\text{N}$  and  $^{15}\text{N}$  chemical shift differences were small, not exceeding 0.003 and 0.02 ppm (Figure 5), respectively. However, large

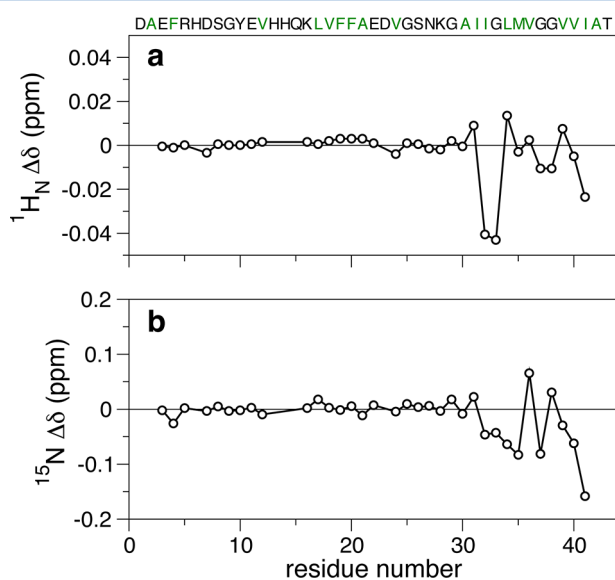


**Figure 5.** Chemical shift differences between monomeric A $\beta$ 42 and A $\beta$ 43 span from residue 31 to the C-terminus. Differences in (a) proton,  $^1\text{H}_\text{N}$   $\Delta\delta$ , and (b) nitrogen,  $^{15}\text{N}$   $\Delta\delta$ , chemical shifts between A $\beta$ 43 and A $\beta$ 42. Large changes in chemical shifts for residue A42 in A $\beta$ 42 and A $\beta$ 43 due to terminal effects are not shown.

differences were observed across the C-terminal region with  $^1\text{H}_\text{N}$  and  $^{15}\text{N}$   $\Delta\delta$  values for residues I32 and G33 exceeding  $-0.04$  ppm. Given the long sequence distance between residues I32 and G33 and the A $\beta$ 43 C-terminus, the large  $\Delta\delta$  values for these residues are unlikely to result from a peptide conformation-independent mechanism,<sup>37</sup> suggesting that the A $\beta$ 43 C-terminal structural ensemble is distinct from that of A $\beta$ 42. Further supporting this hypothesis that the chemical shift differences between A $\beta$ 43 and A $\beta$ 42 are caused by differences in the structural ensemble, C-terminal chemical shift differences between A $\beta$ 43 and A $\beta$ 42 are preserved at 37 °C and are decreased by a factor of approximately 2 under denaturing conditions (Figure S4 of the Supporting Information).

To investigate if differences in local secondary structure contribute to the  $^1\text{H}_\text{N}$  chemical shift differences observed between A $\beta$ 43 and A $\beta$ 42,  $^3J_{\text{HN-H}\alpha}$  coupling constants sensitive to backbone  $\phi$  angles were obtained by line-shape analysis of high-resolution  $^1\text{H}$  HSQC spectra. Our measured  $^3J_{\text{HN-H}\alpha}$  couplings correlate extremely well with previously reported

$^3J_{\text{HN-H}\alpha}$  values for A $\beta$ 40 and A $\beta$ 42 (Figure S5 of the Supporting Information)<sup>38</sup> and are similar for A $\beta$ 40, A $\beta$ 42, and A $\beta$ 43 throughout the majority of the peptide (residues E3–V39). However,  $^3J_{\text{HN-H}\alpha}$  couplings differ at the C-terminus of each peptide at both 10 °C (Figure 6) and 37 °C (Figure S6 of the

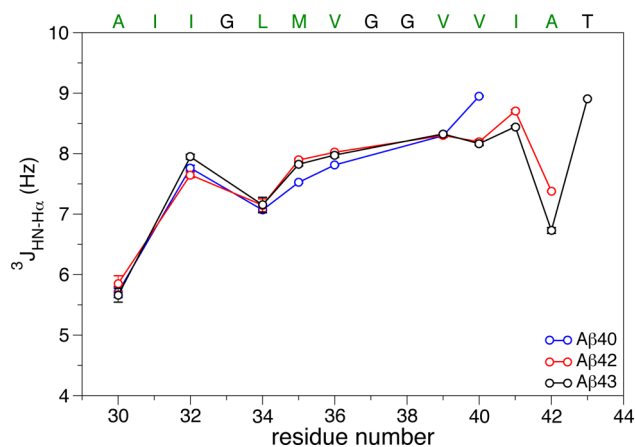


**Figure 6.**  $^3J_{\text{HN-H}\alpha}$  couplings for residues A30 through the C-terminus of A $\beta$ 40 (blue), A $\beta$ 42 (red), and A $\beta$ 43 (black). Error bars denote the standard deviation.

Supporting Information). The near-maximal possible  $^3J_{\text{HN-H}\alpha}$  value of T43 (8.9 Hz) demonstrates that the terminal residue of A $\beta$ 43 adopts a  $\phi$  angle near  $-120^\circ$  far more often than the terminal alanine of A $\beta$ 42 with a  $^3J_{\text{HN-H}\alpha}$  value of 7.4 Hz. This difference is likely due to the increased extended conformation propensity due to branching at C $\beta$ .<sup>39</sup> However,  $^{13}\text{C}\alpha$ ,  $^{13}\text{C}\beta$ ,  $^1\text{H}\alpha$ , and  $^1\text{H}\beta$  and chemical shifts for the C-termini of A $\beta$ 42 and A $\beta$ 43 from natural abundance  $^1\text{H}$ – $^{13}\text{C}$  HSQC spectra (Figure S7 of the Supporting Information) demonstrate no significant shift differences in resolvable nonterminal residues except a 0.2 ppm upfield C $\alpha$  shift for I41, consistent with a slightly lower helical or higher extended/coil propensity based on refDB statistics for Ile.<sup>40</sup> Taken together, significant dynamical differences across the C-terminus and measurable differences in  $^1\text{H}_\text{N}$  and  $^{15}\text{N}$  chemical shifts without hallmarks of the formation of stable secondary structure (e.g., increased level of chemical shift dispersion and changes in C $\alpha$  and C $\beta$  chemical shifts, large differences in  $^3J_{\text{HN-H}\alpha}$ ) suggest that addition of T43 changes the population of transiently formed structure in the C-terminal region of monomeric A $\beta$ .

**Structure and Dynamics in Protofibril-Bound States of A $\beta$ 43.** Because our previous work demonstrated that the additional residues in A $\beta$ 42 led to motions in the protofibril-bound state slower than those of A $\beta$ 40, we used the same combination of  $^{15}\text{N}$   $\Delta R_2$  and DEST NMR to determine if the additional threonine in A $\beta$ 43 also demonstrated slowed C-terminal dynamics in the protofibril-bound state. By measurement of the difference between transverse relaxation rates,  $^{15}\text{N}$   $\Delta R_2$ , in the presence of A $\beta$ 43 protofibrils (high concentration, 120  $\mu\text{M}$ ) and in a low-concentration reference sample without protofibrils (25  $\mu\text{M}$ ), a residue-by-residue picture of the interactions stabilizing binding of A $\beta$ 43 to protofibrils begins to emerge. In-phase  $^{15}\text{N}$   $R_2$  values for 25  $\mu\text{M}$  A $\beta$ 43 range from  $1.60 \pm 0.03$  to  $5.6 \pm 0.2$  s $^{-1}$ , representing those expected for a peptide of this size under these conditions. For samples of 120  $\mu\text{M}$  total A $\beta$ 43, where approximately 10% of the peptide remains monomeric,  $R_2$  values are consistently higher, from 2.8



$\pm 0.1$  to  $8.0 \pm 0.6 \text{ s}^{-1}$ . It is important to note that the smooth variation in  $\Delta R_2$  from position to position observed here (Figure 7a) and the external field and nucleus ( $^{15}\text{N}$  vs  $^1\text{H}_\text{N}$ )

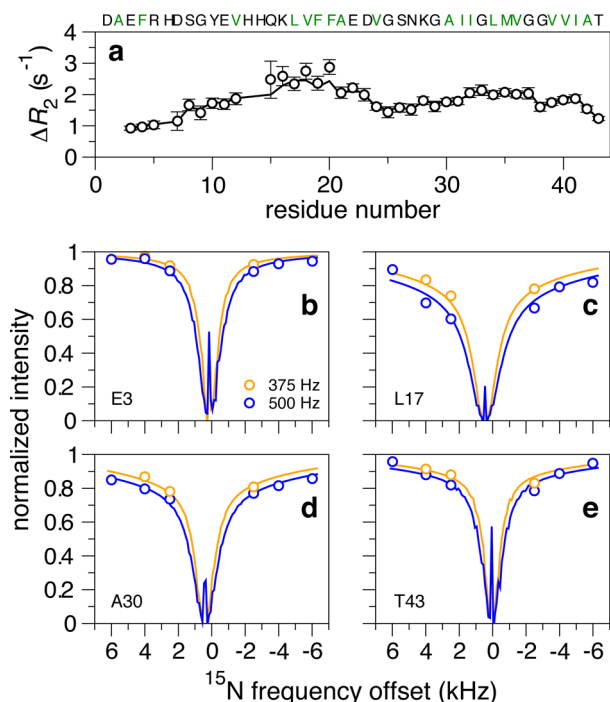


**Figure 7.** Protofibril-bound state of  $A\beta$ 43 probed at atomic resolution by  $^{15}\text{N}$   $\Delta R_2$  and dark-state exchange saturation transfer (DEST) NMR spectroscopy. (a) The enhancements in  $^{15}\text{N}$  transverse relaxation rates [ $^{15}\text{N}$   $\Delta R_2$  (O)] of  $120 \mu\text{M}$   $A\beta$ 43 compared to those of  $25 \mu\text{M}$  samples arise due to interactions of the NMR visible monomeric peptide with the protofibrils. The best-fit  $^{15}\text{N}$   $\Delta R_2$  is illustrated with the solid black line. (b–e)  $^{15}\text{N}$  DEST experiments. The normalized intensity of  $A\beta$ 43 monomer resonances as a function of saturation at kilohertz offsets from the  $^{15}\text{N}$  carrier frequency (119 ppm). Radiofrequency fields of 500 and 375 Hz at frequency offsets from 6 to  $-6$  kHz were used to saturate the protofibrillar dark state with single-residue specificity, shown for residues E3, L17, A30, and T43. Lines indicate the calculated saturation profiles using the best-fit parameters for a  $^{15}\text{N}$  spin in a model incorporating both tethered and direct contact states. Error bars denote the standard deviation.

independence we described previously for  $A\beta$ 40 and  $A\beta$ 42 under these conditions indicate that  $\Delta R_2$  does not arise from intermediate time scale chemical exchange broadening, but rather a lifetime broadening effect due to binding of the NMR visible monomer to the very high-molecular weight ( $>2$  MDa) protofibril where transverse  $^{15}\text{N}$  magnetization relaxes rapidly (faster than the rate of unbinding).<sup>41</sup> In the case of  $A\beta$ 43, the maximal  $\Delta R_2$  of  $2.9 \pm 0.2 \text{ s}^{-1}$  (Figure 7a) represents instead the apparent first-order association rate constant ( $k_{\text{on}}^{\text{app}}$ ) for binding. This finding is similar to the previously reported values for  $A\beta$ 40 ( $3.0 \pm 0.2 \text{ s}^{-1}$ ) at  $270 \mu\text{M}$  and  $A\beta$ 42 ( $2.4 \pm 0.2 \text{ s}^{-1}$ ) at  $150 \mu\text{M}$ .<sup>26</sup>

Residue-by-residue behavior in the protofibril-bound state in exchange with the population of monomers of  $A\beta$ 43 can be probed directly using DEST NMR. The experiment can be summarized as follows. Longitudinal  $^{15}\text{N}$  magnetization prepared in the DEST experiment is efficiently saturated by weak, off-resonance, continuous wave pulses only in the slowly tumbling protofibrils; the monomer is largely unaffected. This saturation is then transferred to the pool of monomers when

peptides unbind from the aggregates. The subsequent attenuation of the monomeric  $A\beta$ 43 resonances is residue-specific (Figure 7b–e). The attenuation varies on the basis of the conformation and motions in the protofibrillar state, with greater attenuation observed for slower moving regions, revealing structural and dynamic details of the protofibril-bound state.

An atomically detailed model of the dynamic binding of  $A\beta$  peptides to protofibrils can be created by combining the results of DEST NMR and  $\Delta R_2$  experiments, as we have recently demonstrated for  $A\beta$ 40 and  $A\beta$ 42.<sup>26</sup> As was the case for  $A\beta$ 40 and  $A\beta$ 42, a two-state model with a single protofibril-bound state, where each residue has a unique fit parameter for  $R_2$  in the bound state, cannot fit all the data simultaneously. However, the DEST and  $\Delta R_2$  data are consistent with a simple modification to the two-state model where each residue in the protofibril-bound state can be in direct contact with the aggregate surface or tethered to the surface by the binding of residues further down the chain (Figure 8a). In this model, each residue experiences the same transverse relaxation rate when in direct contact with the surface,  $R_2^{\text{contact}}$ , reflecting the common, slow motions of the protofibril, and two residue-specific properties: the ratio of the time spent in direct-contact states versus states tethered to the surface via the direct interactions of other residues in the same chain,  $K_3$ , and the average transverse relaxation rate when tethered,  $^{15}\text{N}$   $R_2^{\text{tethered}}$ . This model adds the fewest number of parameters to a two-state model that allows a good fit to the experimental data.<sup>26</sup> The first-order rate constant describing the binding of the monomer to the protofibril,  $k_{\text{on}}^{\text{app}}$ , is set to  $3 \text{ s}^{-1}$ , the maximal value of  $\Delta R_2$ . Because the low equilibrium monomer concentration ( $12 \mu\text{M}$ ) and accompanying low signal-to-noise ratio limited the number of high-quality data points that can be measured in a 5 day DEST experiment compared to that previously measured for  $A\beta$ 40 and  $A\beta$ 42, the global kinetic parameters relating the binding and unbinding of  $A\beta$  from the protofibrils at equilibrium could not be uniquely determined from the DEST and  $\Delta R_2$  data.  $R_2^{\text{contact}}$  is consistent with a single, residue-independent value ranging from  $10000$  to  $30000 \text{ s}^{-1}$  and was set to  $19000 \text{ s}^{-1}$  to match the values previously determined for  $A\beta$ 40 and  $A\beta$ 42.<sup>26</sup> The population of transiently protofibril-bound monomer,  $p_{\text{B}}$ , is consistent with values from 2 to 10%. Choosing a value of 4%, the same as that for  $A\beta$ 42 and similar to that for  $A\beta$ 40 (6%), in combination with an  $R_2^{\text{contact}}$  of  $19000 \text{ s}^{-1}$  results in N-terminal values of residue-specific  $R_2^{\text{tethered}}$  similar to those for both  $A\beta$ 40 and  $A\beta$ 42, and hence this choice was made for further analysis. Although the values of  $R_2^{\text{contact}}$  and  $p_{\text{B}}$  affect the quantitative values of the residue-specific parameters, the interpretation of the data is independent of the chosen values (see Figure S8 of the Supporting Information).

The simple extension to the two-state model captures an atomic level picture of the dynamic ensemble of protofibril-bound structures in two residue-specific parameters,  $K_3$  and  $R_2^{\text{tethered}}$ .  $K_3$ , measuring the ratio of direct contact to tethered states at any given residue, for  $A\beta$ 43 is highest across residues 17–21 and residues 30–36 (Figure 8b), which comprise the central and C-terminal hydrophobic regions of the peptide, respectively, indicating that these residues are most likely to bind directly to the protofibril surface. In contrast, lower values of  $K_3$  are found at the hydrophilic regions at the N-terminus and the region connecting the hydrophobic patches. This pattern is similar to that found for  $A\beta$ 40 and  $A\beta$ 42. The average

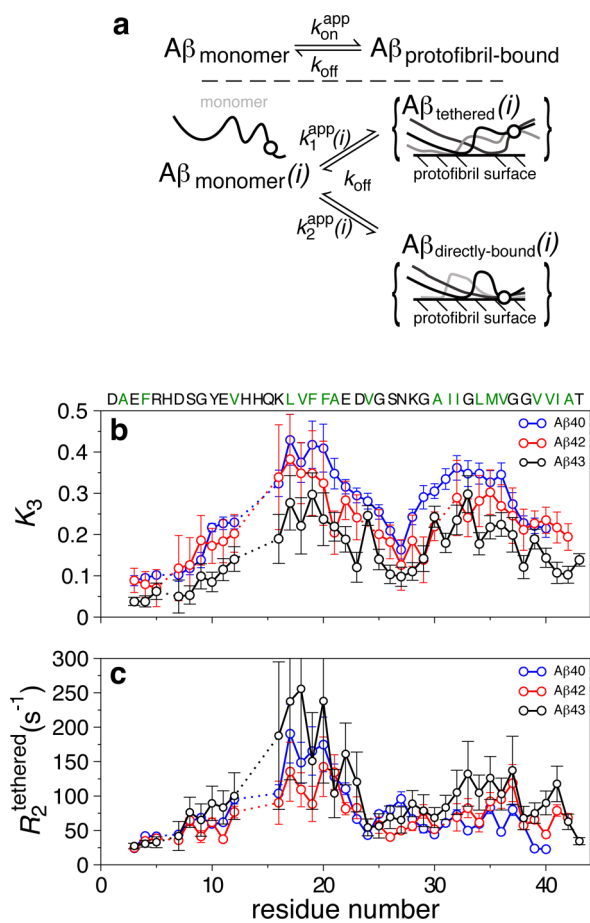


**Figure 8.** Binding model and local parameters describing *Aβ*43 monomer–protofibril interactions. (a) The dynamic binding of *Aβ*43 to protofibrils can be described by a model incorporating two different ensembles of states for each residue: in direct contact with the surface or tethered via the binding of other residues. (b) Residue-specific equilibrium constant ( $K_3$ ) values for *Aβ*40 (blue), *Aβ*42 (red), and *Aβ*43 (black) describing the relative ratio of direct contact and tethered states for each residue. (c) Residue-specific  $^{15}\text{N}$   $R_2^{\text{tethered}}$  values for *Aβ*40 (blue), *Aβ*42 (red), and *Aβ*43 (black) describing the average structure and motions of each residue when it is tethered to protofibrils by the binding of other residues in the same chain. Error bars denote the standard deviation. Values presented for *Aβ*40 and *Aβ*42 were taken from ref 26.

value of  $K_3$  for *Aβ*43 for the fit parameters described above is lower than that of *Aβ*42, which is lower than that of *Aβ*40. This inverse dependence on *Aβ* length is likely a result of an increasing level of competition between additional protofibril-binding sites on the *Aβ* peptide with an increasing length. Unlike both *Aβ*42 and *Aβ*40 where the value of  $K_3$  falls at the C-terminus, the value of  $K_3$  rises at T43, indicating that the terminal threonine of *Aβ*43 plays a role in directly mediating contact with protofibrillar aggregates.

The residue-specific values of  $R_2^{\text{tethered}}$  provide a quantitative measure of the average motions of each residue of *Aβ*43 when it is tethered to the protofibril surface (Figure 8c). Larger values of  $R_2^{\text{tethered}}$  correspond to slower motions, most likely due to shorter tethering lengths. As previously observed for *Aβ*40 and *Aβ*42,  $R_2^{\text{tethered}}$  values for *Aβ*43 are lowest in the hydrophilic N-terminal region, suggesting they are most often far from the aggregate surface when other residues mediate direct interaction.  $R_2^{\text{tethered}}$  values are higher in hydrophobic regions

and closely match those of *Aβ*42, showing significantly slower motions than *Aβ*40 in the C-terminal hydrophobic region. Taken together, these data suggest protofibril-bound states of *Aβ*43 are structurally and dynamically more similar to those of *Aβ*42 than those of *Aβ*40, with additional interactions in the protofibril-bound state mediated directly by T43.

**DISCUSSION**

Recent evidence points to the potential of *Aβ* peptides other than the most common *Aβ*40 and *Aβ*42 to seed toxic aggregates in AD.<sup>32</sup> Among these low-population species, *Aβ*43 is of particular interest because its aggregation is a hallmark of sporadic AD,<sup>30</sup> the most common form of AD, whose molecular origins are currently unknown.

Here, we characterized the changes in the aggregation and structural properties of the *Aβ* peptide introduced by the addition of a single C-terminal threonine residue to form *Aβ*43. This terminal extension alters the structure and dynamics of both the monomeric state and the resulting protofibrillar aggregates. In the monomeric state, slower motions that cannot be explained simply by a longer peptide are evident across the C-terminus of *Aβ*43 relative to *Aβ*42 (Figure 4), supporting the hypothesis of Wang and co-workers that slower motions in the monomeric state of *Aβ* are correlated with a higher aggregation propensity.<sup>12</sup> These dynamical differences are accompanied by differences in chemical shifts (Figure 5 and Figure S7 of the Supporting Information), suggesting that slower motions in *Aβ*43 can be attributed to a distinct structural ensemble compared to that of *Aβ*42. Although the structural ensemble is difficult to determine directly because of the extremely low equilibrium concentration (12  $\mu\text{M}$ ), *Aβ*43 chemical shifts are consistent with a highly disordered protein as is observed for *Aβ*40 and *Aβ*42,<sup>13,42</sup> though small chemical shift differences across the C-terminus likely arise from changes in transiently populated structures (e.g., hydrogen-bonded turns). Differences in the monomeric state are mirrored in the aggregation of *Aβ*43, which more rapidly forms protofibrils and has a critical aggregation concentration much lower than those of *Aβ*42 and *Aβ*40 (Figure 2). In the protofibril-bound state, the slow dynamics of the C-terminal residues when they are tethered and the partitioning into tethered and directly bound states of *Aβ*43 more closely resemble those of *Aβ*42 than those of *Aβ*40, demonstrating a correlation between the aggregation behavior and the dynamics in the protofibril-bound state. In addition, the C-terminus of *Aβ*43 is involved in direct contact with the aggregates more often than the adjacent residues, unlike at the termini of *Aβ*40 and *Aβ*42. Stabilizing contacts between the C-terminal ends of *Aβ* peptides at the core of transient oligomeric aggregates are critical for overcoming the critical nucleus for formation of partially ordered stable aggregates including protofibrils.<sup>43</sup> Hence, the direct contacts formed by the C-terminal threonine may provide an explanation for the protofibril formation of *Aβ*43 being much more rapid than that of *Aβ*42. In summary, these results support the hypothesis that small but significant differences in the monomeric and protofibrillar structure and dynamics of *Aβ*43 result in an increased aggregation propensity, providing an explanation for the observed enhanced toxicity of *Aβ*43 and a possible mechanism for its suspected role in sporadic AD.

The correlation between C-terminal *Aβ* length and aggregation propensity has been studied extensively, primarily comparing the most common species, *Aβ*40 and *Aβ*42. Lansbury and co-workers demonstrated that C-terminal



fragments of long  $A\beta$  species,  $A\beta_{26-42}$  and  $A\beta_{26-43}$ , showed aggregation much more rapid than that of  $A\beta_{26-40}$  but could not resolve a difference between these species.<sup>9</sup> Similarly, Vandersteen et al. demonstrate that  $A\beta_{43}$  and  $A\beta_{42}$  both aggregate rapidly, without a distinct lag phase in fibril formation monitored by thioflavin T fluorescence, but could not quantitatively distinguish the aggregation rates of  $A\beta_{42}$  from  $A\beta_{43}$ .<sup>32</sup> We have shown that  $A\beta_{43}$  does dramatically increase the rate and extent of protofibril aggregation relative to those of  $A\beta_{42}$ . Our results demonstrate that this higher aggregation propensity is associated with slower motions in both the monomeric and protofibril-bound states. Furthermore, our data attribute this difference in dynamics to small but critical structural changes in the C-terminal structural ensemble, similar to the significant structural differences observed for  $A\beta_{42}$  due to the two additional residues present relative to  $A\beta_{40}$ .<sup>44</sup> Although our results probe the structure, motions, and aggregation of  $A\beta_{43}$  at atomic resolution, future studies using molecular simulation may shed light on the specific contacts stabilized by T43 in the monomeric and protofibril-bound state that are difficult to exhaustively characterize using experiments alone. The differences between the chemical shifts,  $R_2$ , and DEST parameters of  $A\beta_{43}$  relative to those of  $A\beta_{42}$  reported here will serve as important residue-specific observables for direct validation of both the structure and dynamics of simulated ensembles, as we have previously demonstrated for shorter  $A\beta$  peptides.<sup>35,45</sup>

Although high-resolution NMR experiments offer the ability to study the structure and aggregation of  $A\beta$  peptides with atomistic precision, the conditions used here are entirely *in vitro* under a single set of conditions, and the behavior under other conditions as well as *in vivo* may be different. One important difference between these experimental conditions commonly used for *in vitro* studies and the native environment is the concentration of  $A\beta$ ; while we used concentrations of  $>10 \mu\text{M}$ ,  $A\beta$  peptides are typically present at concentrations of  $\sim 25 \text{ nM}$ . However, the native environment is not homogeneous, and recent work suggests that aggregation is initiated within endosomes that concentrate  $A\beta$  to the micromolar range, leading to subsequent seeding of extracellular amyloid formation.<sup>46</sup> Hence, the concentrations used for this work potentially correspond to the effective conditions *in vivo*; the critical concentration in the low micromolar range and more rapid aggregation of  $A\beta_{43}$ , compared to that of  $A\beta_{42}$ , lead us to hypothesize that  $A\beta_{43}$  is able to nucleate toxic aggregates in endocytic compartments much more frequently than shorter  $A\beta$  species. Therefore, we propose a model in which  $A\beta_{43}$  aggregates either with itself or with other highly aggregation-prone  $A\beta$  variants to seed subsequent  $A\beta_{42}$  aggregation. The biochemical changes that lead to even a small increase in the level of production of  $A\beta_{43}$ , because of impaired  $\gamma$ -secretase activity along the pathway to form  $A\beta_{40}$ , may be a critical trigger for AD. Additionally, therapeutic strategies attempting to clear  $A\beta$  using either active ( $A\beta$  immunization) or passive (administration of  $A\beta$ -binding antibodies) targeting specifically  $A\beta_{43}$  should be investigated. For example, in the mouse model of Saito et al. where  $A\beta_{43}$  is overproduced because of a mutation, the ability of an  $A\beta_{43}$ -specific immunotherapy to prevent both plaque formation and the observed neurological deficits could be tested. Further experiments to test the hypothesis that  $A\beta_{43}$  recruits  $A\beta_{42}$  aggregation *in vitro* by determining the aggregation rates and atomic resolution

mechanism of co-aggregation in mixtures of  $A\beta$  peptides containing  $A\beta_{43}$  are ongoing in the laboratory.

## ■ ASSOCIATED CONTENT

### 📄 Supporting Information

The 37 °C aggregation time course and TEM imaging; overlay of  $^{15}\text{N}$   $R_2$  values for  $A\beta_{43}$  measured at 15 and 25  $\mu\text{M}$  and for  $A\beta_{43}$  and  $A\beta_{42}$  measured under denaturing conditions; overlay of chemical shift differences between  $A\beta_{43}$  and  $A\beta_{42}$  observed under native conditions (10 and 37 °C) and denaturing conditions; correlation plot of  $^3J_{\text{HN-H}\alpha}$  values measured by line-shape analysis and reported previously; overlay of  $^3J_{\text{HN-H}\alpha}$  values at 10 and 37 °C;  $C\alpha$  region of  $^1\text{H}$ - $^{13}\text{C}$  HSQC of  $A\beta_{42}$  and  $A\beta_{43}$ ; and comparison of the effect of  $p_B$  values on best-fit residue-specific parameters. This material is available free of charge via the Internet at <http://pubs.acs.org>.

## ■ AUTHOR INFORMATION

### Corresponding Author

\*Address: 70 Ship St., Box G-E, Providence, RI 02912. E-mail: Nicolas\_Fawzi@brown.edu. Phone: (401) 863-5232.

### Funding

Research reported in this publication was supported in part by a pilot project award to N.L.F. as part of an Institutional Development Award (IDeA) from the National Institute of General Medical Sciences of the National Institutes of Health via Grant 5 P20 GM103430-13. A.E.C. was a predoctoral trainee supported in part by Grant T32-GM07601. This research is based in part upon work conducted using the Rhode Island NSF/EPSCoR Proteomics Shared Resource Facility, which is supported in part by National Science Foundation EPSCoR Grant 1004057, National Institutes of Health Grant 1S10RR020923, a Rhode Island Science and Technology Advisory Council grant, and the Division of Biology and Medicine, Brown University. This research is based in part on data obtained at the Brown University Structural Biology Core Facility, which is supported by the Division of Biology and Medicine, Brown University.

### Notes

The authors declare no competing financial interest.

## ■ ACKNOWLEDGMENTS

We thank Michael “Sparky” Clarkson for technical assistance and helpful conversations, Art Salomon for use of lyophilization equipment, Rute Silva for wet laboratory assistance, Jinfa Ying and David Libich for helpful discussions regarding scalar coupling and chemical shift measurements, and Geoff Williams and the Leduc Bioimaging Facility at Brown University for assistance with the transmission electron microscopy described in this study. We also thank the Center for Computation and Visualization at Brown University for providing the computational resources required for running the DESTfit software. We thank Chunyu Wang and David Rosenman for providing their published experimental  $^3J_{\text{HN-H}\alpha}$  data.

## ■ ABBREVIATIONS

NMR, nuclear magnetic resonance; AD, Alzheimer’s disease; FAD, familial Alzheimer’s disease;  $A\beta$ , amyloid  $\beta$ ; DEST, dark-state exchange saturation transfer; HSQC, heteronuclear single-quantum coherence; TEM, transmission electron microscopy;  $R_1$ , longitudinal relaxation rate constant;  $R_2$ , transverse relaxation rate constant; CPMG, Carr–Purcell–Meiboom–

Gill; NOE, nuclear Overhauser effect;  $^3J_{\text{HN-H}\alpha}$  three-bond (HN-H $\alpha$ ) scalar coupling constant.

## REFERENCES

- (1) Hardy, J., and Selkoe, D. J. (2002) The amyloid hypothesis of Alzheimer's disease: Progress and problems on the road to therapeutics. *Science* 297, 353–356.
- (2) Dickson, D. W., Crystal, H. A., Bevana, C., Honer, W., Vincent, I., and Davies, P. (1995) Correlations of synaptic and pathological markers with cognition of the elderly. *Neurobiol. Aging* 16, 285–298, 298–304 (discussion).
- (3) McLean, C. A., Cherny, R. A., Fraser, F. W., Fuller, S. J., Smith, M. J., Beyreuther, K., Bush, A. I., and Masters, C. L. (1999) Soluble pool of A $\beta$  amyloid as a determinant of severity of neurodegeneration in Alzheimer's disease. *Ann. Neurol.* 46, 860–866.
- (4) Walsh, D. M., Hartley, D. M., Kusumoto, Y., Fezoui, Y., Condron, M. M., Lomakin, A., Benedek, G. B., Selkoe, D. J., and Teplow, D. B. (1999) Amyloid  $\beta$ -protein fibrillogenesis. Structure and biological activity of protofibrillar intermediates. *J. Biol. Chem.* 274, 25945–25952.
- (5) Lue, L. F., Kuo, Y. M., Roher, A. E., Brachova, L., Shen, Y., Sue, L., Beach, T., Kurth, J. H., Rydel, R. E., and Rogers, J. (1999) Soluble amyloid  $\beta$  peptide concentration as a predictor of synaptic change in Alzheimer's disease. *Am. J. Pathol.* 155, 853–862.
- (6) Benilova, I., Karran, E., and De Strooper, B. (2012) The toxic A $\beta$  oligomer and Alzheimer's disease: An emperor in need of clothes. *Nat. Neurosci.* 15, 349–357.
- (7) Zhao, G., Mao, G., Tan, J., Dong, Y., Cui, M. Z., Kim, S. H., and Xu, X. (2004) Identification of a new presenilin-dependent  $\zeta$ -cleavage site within the transmembrane domain of amyloid precursor protein. *J. Biol. Chem.* 279, 50647–50650.
- (8) Steiner, H., Fluhrer, R., and Haass, C. (2008) Intramembrane proteolysis by  $\gamma$ -secretase. *J. Biol. Chem.* 283, 29627–29631.
- (9) Jarrett, J. T., Berger, E. P., and Lansbury, P. T., Jr. (1993) The carboxy terminus of the  $\beta$  amyloid protein is critical for the seeding of amyloid formation: Implications for the pathogenesis of Alzheimer's disease. *Biochemistry* 32, 4693–4697.
- (10) Borchelt, D. R., Thinakaran, G., Eckman, C. B., Lee, M. K., Davenport, F., Ratovitsky, T., Prada, C. M., Kim, G., Seekins, S., Yager, D., Slunt, H. H., Wang, R., Seeger, M., Levey, A. I., Gandy, S. E., Copeland, N. G., Jenkins, N. A., Price, D. L., Younkin, S. G., and Sisodia, S. S. (1996) Familial Alzheimer's disease-linked presenilin 1 variants elevate A $\beta$ 1–42/1–40 ratio in vitro and in vivo. *Neuron* 17, 1005–1013.
- (11) Yan, Y., Liu, J., McCallum, S. A., Yang, D., and Wang, C. (2007) Methyl dynamics of the amyloid- $\beta$  peptides A $\beta$ 40 and A $\beta$ 42. *Biochem. Biophys. Res. Commun.* 362, 410–414.
- (12) Yan, Y., and Wang, C. (2006) A $\beta$ 42 is more rigid than A $\beta$ 40 at the C terminus: Implications for A $\beta$  aggregation and toxicity. *J. Mol. Biol.* 364, 853–862.
- (13) Riek, R., Guntert, P., Dobeli, H., Wipf, B., and Wuthrich, K. (2001) NMR studies in aqueous solution fail to identify significant conformational differences between the monomeric forms of two Alzheimer peptides with widely different plaque-competence, A $\beta$ (1–40)(ox) and A $\beta$ (1–42)(ox). *Eur. J. Biochem.* 268, 5930–5936.
- (14) Lu, J. X., Qiang, W., Yau, W. M., Schwieters, C. D., Meredith, S. C., and Tycko, R. (2013) Molecular structure of  $\beta$ -amyloid fibrils in Alzheimer's disease brain tissue. *Cell* 154, 1257–1268.
- (15) Luhrs, T., Ritter, C., Adrian, M., Riek-Loher, D., Bohrmann, B., Dobeli, H., Schubert, D., and Riek, R. (2005) 3D structure of Alzheimer's amyloid- $\beta$ (1–42) fibrils. *Proc. Natl. Acad. Sci. U.S.A.* 102, 17342–17347.
- (16) Zhang, R., Hu, X., Khant, H., Ludtke, S. J., Chiu, W., Schmid, M. F., Frieden, C., and Lee, J. M. (2009) Interprotofilament interactions between Alzheimer's A $\beta$ 1–42 peptides in amyloid fibrils revealed by cryoEM. *Proc. Natl. Acad. Sci. U.S.A.* 106, 4653–4658.
- (17) Abelein, A., Kaspersen, J. D., Nielsen, S. B., Jensen, G. V., Christiansen, G., Pedersen, J. S., Danielsson, J., Otzen, D. E., and Graslund, A. (2013) Formation of dynamic soluble surfactant-induced amyloid  $\beta$  peptide aggregation intermediates. *J. Biol. Chem.* 288, 23518–23528.
- (18) Ladiwala, A. R., Litt, J., Kane, R. S., Aucoin, D. S., Smith, S. O., Ranjan, S., Davis, J., Van Nostrand, W. E., and Tessier, P. M. (2012) Conformational differences between two amyloid  $\beta$  oligomers of similar size and dissimilar toxicity. *J. Biol. Chem.* 287, 24765–24773.
- (19) Ahmed, M., Davis, J., Aucoin, D., Sato, T., Ahuja, S., Aimoto, S., Elliott, J. L., Van Nostrand, W. E., and Smith, S. O. (2010) Structural conversion of neurotoxic amyloid- $\beta$ (1–42) oligomers to fibrils. *Nat. Struct. Mol. Biol.* 17, 561–567.
- (20) Carulla, N., Zhou, M., Arimon, M., Gairi, M., Giralt, E., Robinson, C. V., and Dobson, C. M. (2009) Experimental characterization of disordered and ordered aggregates populated during the process of amyloid fibril formation. *Proc. Natl. Acad. Sci. U.S.A.* 106, 7828–7833.
- (21) Scheidt, H. A., Morgado, I., and Huster, D. (2012) Solid-state NMR reveals a close structural relationship between amyloid- $\beta$  protofibrils and oligomers. *J. Biol. Chem.* 287, 22822–22826.
- (22) Bertini, I., Gallo, G., Korsak, M., Luchinat, C., Mao, J., and Ravera, E. (2013) Formation kinetics and structural features of  $\beta$ -amyloid aggregates by sedimented solute NMR. *ChemBioChem* 14, 1891–1897.
- (23) Narayanan, S., and Reif, B. (2005) Characterization of chemical exchange between soluble and aggregated states of  $\beta$ -amyloid by solution-state NMR upon variation of salt conditions. *Biochemistry* 44, 1444–1452.
- (24) Dasari, M., Espargaro, A., Sabate, R., Lopez del Amo, J. M., Fink, U., Grelle, G., Bieschke, J., Ventura, S., and Reif, B. (2011) Bacterial inclusion bodies of Alzheimer's disease  $\beta$ -amyloid peptides can be employed to study native-like aggregation intermediate states. *ChemBioChem* 12, 407–423.
- (25) Krishnamoorthy, J., Brender, J. R., Vivekanandan, S., Jahr, N., and Ramamoorthy, A. (2012) Side-chain dynamics reveals transient association of A $\beta$ (1–40) monomers with amyloid fibers. *J. Phys. Chem. B* 116, 13618–13623.
- (26) Fawzi, N. L., Ying, J., Ghirlando, R., Torchia, D. A., and Clore, G. M. (2011) Atomic-resolution dynamics on the surface of amyloid- $\beta$  protofibrils probed by solution NMR. *Nature* 480, 268–272.
- (27) Jawhar, S., Wirths, O., and Bayer, T. A. (2011) Pyroglutamate amyloid- $\beta$  (A $\beta$ ): A hatchet man in Alzheimer disease. *J. Biol. Chem.* 286, 38825–38832.
- (28) Saito, T., Suemoto, T., Brouwers, N., Slegers, K., Funamoto, S., Mihira, N., Matsuba, Y., Yamada, K., Nilsson, P., Takano, J., Nishimura, M., Iwata, N., Van Broeckhoven, C., Ihara, Y., and Saido, T. C. (2011) Potent amyloidogenicity and pathogenicity of A $\beta$ 43. *Nat. Neurosci.* 14, 1023–1032.
- (29) Welander, H., Franberg, J., Graff, C., Sundstrom, E., Winblad, B., and Tjernberg, L. O. (2009) A $\beta$ 43 is more frequent than A $\beta$ 40 in amyloid plaque cores from Alzheimer disease brains. *J. Neurochem.* 110, 697–706.
- (30) Sandebring, A., Welander, H., Winblad, B., Graff, C., and Tjernberg, L. O. (2013) The pathogenic A $\beta$ 43 is enriched in familial and sporadic Alzheimer disease. *PLoS One* 8, e55847.
- (31) Zou, K., Liu, J., Watanabe, A., Hiraga, S., Liu, S., Tanabe, C., Maeda, T., Terayama, Y., Takahashi, S., Michikawa, M., and Komano, H. (2013) A $\beta$ 43 is the earliest-depositing A $\beta$  species in APP transgenic mouse brain and is converted to A $\beta$ 41 by two active domains of ACE. *Am. J. Pathol.* 182, 2322–2331.
- (32) Vandersteent, A., Masman, M. F., De Baets, G., Jonckheere, W., van der Werf, K., Marrink, S. J., Rozenski, J., Benilova, I., De Strooper, B., Subramaniam, V., Schymkowitz, J., Rousseau, F., and Broersen, K. (2012) Molecular plasticity regulates oligomerization and cytotoxicity of the multipetide-length amyloid- $\beta$  peptide pool. *J. Biol. Chem.* 287, 36732–36743.
- (33) Delaglio, F., Grzesiek, S., Vuister, G. W., Zhu, G., Pfeifer, J., and Bax, A. (1995) NMRPipe: A multidimensional spectral processing system based on UNIX pipes. *J. Biomol. NMR* 6, 277–293.
- (34) Fawzi, N. L., Ying, J., Torchia, D. A., and Clore, G. M. (2012) Probing exchange kinetics and atomic resolution dynamics in high-

molecular-weight complexes using dark-state exchange saturation transfer NMR spectroscopy. *Nat. Protoc.* 7, 1523–1533.

(35) Fawzi, N. L., Phillips, A. H., Ruscio, J. Z., Doucleff, M., Wemmer, D. E., and Head-Gordon, T. (2008) Structure and dynamics of the A $\beta$ (21–30) peptide from the interplay of NMR experiments and molecular simulations. *J. Am. Chem. Soc.* 130, 6145–6158.

(36) Kragelj, J., Ozenne, V., Blackledge, M., and Jensen, M. R. (2013) Conformational propensities of intrinsically disordered proteins from NMR chemical shifts. *ChemPhysChem* 14, 3034–3045.

(37) Maltsev, A. S., Ying, J., and Bax, A. (2012) Impact of N-terminal acetylation of  $\alpha$ -synuclein on its random coil and lipid binding properties. *Biochemistry* 51, 5004–5013.

(38) Rosenman, D. J., Connors, C. R., Chen, W., Wang, C., and Garcia, A. E. (2013) A $\beta$  monomers transiently sample oligomer and fibril-like configurations: Ensemble characterization using a combined MD/NMR approach. *J. Mol. Biol.* 425, 3338–3359.

(39) Minor, D. L., Jr., and Kim, P. S. (1994) Measurement of the  $\beta$ -sheet-forming propensities of amino acids. *Nature* 367, 660–663.

(40) Zhang, H., Neal, S., and Wishart, D. S. (2003) RefDB: A database of uniformly referenced protein chemical shifts. *J. Biomol. NMR* 25, 173–195.

(41) Fawzi, N. L., Ying, J., Torchia, D. A., and Clore, G. M. (2010) Kinetics of amyloid  $\beta$  monomer-to-oligomer exchange by NMR relaxation. *J. Am. Chem. Soc.* 132, 9948–9951.

(42) Hou, L., Shao, H., Zhang, Y., Li, H., Menon, N. K., Neuhaus, E. B., Brewer, J. M., Byeon, I. J., Ray, D. G., Vitek, M. P., Iwashita, T., Makula, R. A., Przybyla, A. B., and Zagorski, M. G. (2004) Solution NMR studies of the A $\beta$ (1–40) and A $\beta$ (1–42) peptides establish that the Met35 oxidation state affects the mechanism of amyloid formation. *J. Am. Chem. Soc.* 126, 1992–2005.

(43) Fawzi, N. L., Okabe, Y., Yap, E. H., and Head-Gordon, T. (2007) Determining the critical nucleus and mechanism of fibril elongation of the Alzheimer's A $\beta$ (1–40) peptide. *J. Mol. Biol.* 365, 535–550.

(44) Ball, K. A., Phillips, A. H., Wemmer, D. E., and Head-Gordon, T. (2013) Differences in  $\beta$ -strand populations of monomeric A $\beta$ 40 and A $\beta$ 42. *Biophys. J.* 104, 2714–2724.

(45) Ball, K. A., Phillips, A. H., Nerenberg, P. S., Fawzi, N. L., Wemmer, D. E., and Head-Gordon, T. (2011) Homogeneous and heterogeneous tertiary structure ensembles of amyloid- $\beta$  peptides. *Biochemistry* 50, 7612–7628.

(46) Hu, X., Crick, S. L., Bu, G., Frieden, C., Pappu, R. V., and Lee, J. M. (2009) Amyloid seeds formed by cellular uptake, concentration, and aggregation of the amyloid- $\beta$  peptide. *Proc. Natl. Acad. Sci. U.S.A.* 106, 20324–20329.